



Title	Regular flow reversals in Rayleigh-Benard convection in a horizontal magnetic field
Author(s)	Tasaka, Yuji; Igaki, Kazuto; Yanagisawa, Takatoshi; Vogt, Tobias; Zuerner, Till; Eckert, Sven
Citation	Physical review e, 93(4), 043109 <a href="https://doi.org/10.1103/PhysRevE.93.043109">https://doi.org/10.1103/PhysRevE.93.043109</a>
Issue Date	2016-04-08
Doc URL	<a href="http://hdl.handle.net/2115/61875">http://hdl.handle.net/2115/61875</a>
Rights	©2016 American Physical Society
Type	article
File Information	PhysRevE.93.043109.pdf



[Instructions for use](#)

**Regular flow reversals in Rayleigh-Bénard convection in a horizontal magnetic field**

Yuji Tasaka\* and Kazuto Igaki

*Laboratory for Flow Control, Hokkaido University, Sapporo, Japan*

Takatoshi Yanagisawa

*Department of Deep Earth Structure and Dynamics Research, Japan Agency for Marine-Earth Science and Technology (JAMSTEC), Yokosuka, Japan*

Tobias Vogt, Till Zuerner, and Sven Eckert

*Institute of Fluids Dynamics, Helmholtz Zentrum Dresden-Rossendorf (HZDR), Dresden, Germany*

(Received 21 December 2015; published 8 April 2016)

Magnetohydrodynamic Rayleigh-Bénard convection was studied experimentally using a liquid metal inside a box with a square horizontal cross section and aspect ratio of five. Systematic flow measurements were performed by means of ultrasonic velocity profiling that can capture time variations of instantaneous velocity profiles. Applying a horizontal magnetic field organizes the convective motion into a flow pattern of quasi-two-dimensional rolls arranged parallel to the magnetic field. The number of rolls has the tendency to decrease with increasing Rayleigh number  $Ra$  and to increase with increasing Chandrasekhar number  $Q$ . We explored convection regimes in a parameter range, at  $2 \times 10^3 < Q < 10^4$  and  $5 \times 10^3 < Ra < 3 \times 10^5$ , thus extending the regime diagram provided by Yanagisawa *et al.* [T. Yanagisawa *et al.*, *Phys. Rev. E* **88**, 063020 (2013)]. Three regimes were identified, of which the regime of regular flow reversals in which five rolls periodically change the direction of their circulation with gradual skew of the roll axes can be considered as the most remarkable one. The regime appears around a range of  $Ra/Q = 10$ , where irregular flow reversals were observed in Yanagisawa *et al.* We performed the proper orthogonal decomposition (POD) analysis on the spatiotemporal velocity distribution and detected that the regular flow reversals can be interpreted as a periodic emergence of a four-roll state in a dominant five-roll state. The POD analysis also provides the definition of the effective number of rolls as a more objective approach.

DOI: [10.1103/PhysRevE.93.043109](https://doi.org/10.1103/PhysRevE.93.043109)**I. INTRODUCTION****A. Background**

Rayleigh-Bénard convection (RBC), which means natural convection in a fluid layer caused by vertical temperature difference  $\Delta T$ , is a classical long-known problem in fluid mechanics and the underlying mechanism for complex large scale flows occurring in nature and industry. The RBC is governed by the Rayleigh number,  $Ra = \alpha g \Delta T L^3 / \kappa \nu$ , the Prandtl number,  $Pr = \nu / \kappa$ , and the geometry of the fluid vessel, in particular the aspect ratio, where  $\alpha$ ,  $\kappa$ ,  $\nu$  are the volumetric coefficient of thermal expansion, thermal diffusivity, and kinematic viscosity of test fluids, respectively, and  $g$  and  $L$  are the gravity acceleration and height of the fluid layer, respectively. Tuning these parameters and considering additional effects, for example, surface tension, background rotation, etc., provides a variety of complex fluid motions, as considered by many review papers and books [1–5]. One of the prevailing topics in RBC is the existence of random reversals of the large scale circulation in two-dimensional (2D), quasi-2D, and 3D vessels with small aspect ratios around unity, where the development of corner rolls triggers flow reversals. This phenomenon has a high relevance for explaining polarity reversals of the geomagnetic field and changes of wind direction in earth's atmosphere. Various models have been proposed to explain

the nature of such reversals taking account of the randomness from thermal turbulence [6–8].

Flow reversals are also observed in RBC of a liquid metal layer with imposed horizontal magnetic field. In this configuration, the reversals of flow direction of multiple, quasi-two-dimensional rolls arranged parallel to the magnetic field occur via irregular switching between the four-roll and the five-roll states in the vessel [9]. A subsequent paper classified the regimes observed in the same system including the flow reversals and investigated the statistical characteristics of the regimes [10]. One of the typical features is the continuous variation of the mean number of rolls with increasing  $Ra$ , at a fixed Chandrasekhar number,  $Q = B^2 L^2 \sigma / \rho \nu$ , that represents the ratio of the magnetic force to the viscous force, where  $\sigma$  and  $\rho$  are the electric conductivity and density of test fluids, respectively, and  $B$  is the intensity of the applied magnetic field. Fluid layers with a moderate aspect ratio (for instance, five, as considered in this study) are restricted in the adjustment of an integer number of rolls. The condition of noninteger roll numbers can be fulfilled as the time average of recurring transitions between neighboring roll states. Such a behavior satisfies the requirements by magnetohydrodynamics (MHD) as the imposed magnetic field increases the wave number of convection rolls [11,12].

Magnetohydrodynamic (MHD) effects on RBC have been treated theoretically for unbounded fluid layers; see Ref. [13]. In this book, it was stated that the application of a horizontal magnetic field does not affect the onset of convection, while a vertical one increases the critical Rayleigh number for the

\*tasaka@eng.hokudai.ac.jp

onset of convection,  $Ra_c$ . In realistic cases with bounded fluid layers, the horizontal magnetic field increases  $Ra_c$  because of Hartmann braking on the side wall perpendicular to the magnetic field lines [11]. Convection rolls appear at the onset of convection and become aligned along the magnetic field. In this context, the similarity with Taylor-Proudman's theorem in a rotating system was discussed [13]. Linear stability analysis by Burr and Müller [11] predicts an increasing wave number of two-dimensional rolls with increasing  $Q$ . The quasi-two-dimensional constraint with respect to the roll orientation arises from the influence of the Lorentz force, which reorganizes the flow structure in ways that both the global Joule dissipation and global kinetic energy decline in strict accordance with the conservation of linear and angular momentum [14]. The MHD effect on the quasi-two-dimensional rolls can be represented by an enlargement of the stable region of the rolls [15]. Because of the two-dimensional structure of flows dominated by the Lorentz force, the Eckhaus instability, which is by nature of a two-dimensional instability to alter smaller wave numbers into stable larger ones, is not affected by the imposed magnetic field. Apart from that, the boundaries for skewed-varicose and oscillatory instability that are accompanied by three-dimensional motions are largely affected [15].

By monitoring the development of pointwise temperature fluctuations, Burr and Müller [11] observed the transition from a quasi-two-dimensional state to thermal turbulence, which occurs as a result of increasing  $Ra$  at fixed  $Q$ , or decreasing  $Q$  at relatively large  $Ra$ . The transition to thermal turbulence does not proceed straightforwardly, in particular, irregular flow reversals are observed during the process of transition [9]. This demonstrates that new spatiotemporal flow structures may develop on the route toward the thermal turbulence. The investigation of this transition requires capturing spatiotemporal flow information. The opaque nature of liquid metals that are commonly used for MHD experiments impedes detailed investigations of the spatiotemporal structure. Only a few works, using ionic fluid with extremely strong magnetic fields [12] or analyzing the information from the surface of a liquid metal layer [16], have provided meaningful information so far. The recent development of ultrasonic velocity profiling [17,18] overcomes this problem and provides the capabilities to visualize the structure quantitatively by the line measurement of instantaneous velocity profiles. The statistical characteristics of the thermal turbulence in liquid metal layers were evaluated using the ultrasonic velocity profiling [19,20]. Moreover, a variety of flow regimes, including irregular flow reversals and corresponding statistical characteristics, was uncovered in MHD-RBC [9,10].

### B. Objectives

The primary goal of this study is the enlargement of the parameter area for MHD-RBC in a horizontal magnetic field that was investigated in Yanagisawa *et al.* [9,10] in the range of relatively small  $Q$  numbers,  $Q < 10^3$ . Moreover, detailed investigations of the regime of regular flow reversals have been performed where the special focus was on providing an understanding of the source of irregularity in comparison with reversals observed in large scale circulation (LSC). A description of the experimental setup, measurement tools, and

procedures can be found in Sec. II, and an extended regime diagram containing the observed regimes including regular flow reversals is presented in Sec. III. Proper orthogonal decomposition (POD) analysis on spatiotemporal velocity maps was performed to investigate spatiotemporal characteristics of the flow regimes, especially for the phenomena of regular and irregular flow reversals. The corresponding results are shown and discussed in Sec. IV. Additionally, an evaluation scheme of the effective roll number for the respective regimes is proposed on the basis of the POD analysis.

## II. EXPERIMENTAL SETUP AND MEASUREMENTS

Figure 1 shows the experimental setup, namely, the vessel containing the fluid layer and the arrangement of diverse ultrasonic sensors. The vessel was used in our previous works [9,10]. It consists of two copper plates at the top and the bottom of the cell for ensuring isothermal heating and cooling conditions, whereas Teflon is used for the side walls in order to achieve both thermal and electric insulation. The fluid layer has a square horizontal cross section of  $200 \times 200 \text{ mm}^2$  and a height of  $L = 40 \text{ mm}$  corresponding to an aspect ratio of 5. Most of the experiments were performed at Helmholtz Zentrum Dresden-Rossendorf (HZDR) using the ternary alloy  $\text{Ga}^{67}\text{In}^{20.5}\text{Sn}^{12.5}$  as the test fluid and an electromagnet consisting of two water-cooled copper coils and a magnetic yoke. Supplementary measurements were done at Hokkaido University in liquid gallium by means of a different magnetic coil system with a yoke. The first generator can provide a strong magnetic field up to 700 mT at a uniformity

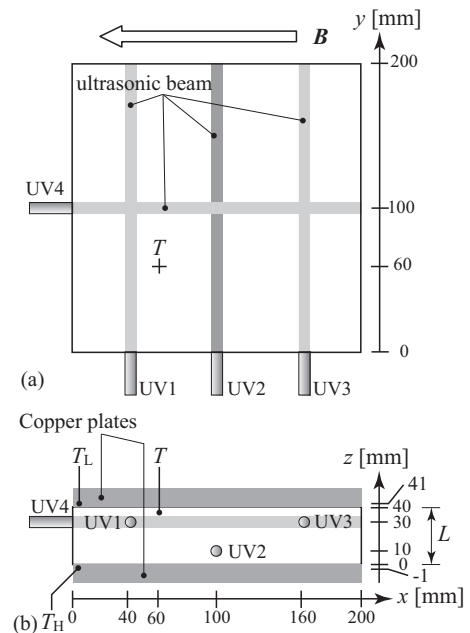


FIG. 1. Schematic view of the fluid layer and the sensor arrangement: (a) top view and (b) side view, where UV1–UV4 and gray lines represent the positions of the ultrasonic transducers and corresponding ultrasonic beam lines. The dark gray line indicates the beam for measurements of the velocity near the bottom plate, whereas the light gray lines show the measuring lines near the top plate. The vertical positions of the sensors were chosen at a distance of 10 mm from the top or the bottom plate, respectively.

TABLE I. Physical properties of Ga<sup>67</sup>In<sup>20.5</sup>Sn<sup>12.5</sup> and liquid gallium [21–25].

Physical properties	Symbol	Unit	GaInSn (25 °C)	Gallium (32 °C)
Thermal expansion coefficient	$\alpha$	K <sup>-1</sup>	$1.02 \times 10^{-4}$	$1.27 \times 10^{-4}$
Thermal diffusivity	$\kappa$	m <sup>2</sup> /s	$1.22 \times 10^{-5}$	$1.27 \times 10^{-5a}$
Kinematic viscosity	$\nu$	m <sup>2</sup> /s	$3.32 \times 10^{-7}$	$3.05 \times 10^{-7}$
Density	kg/m <sup>3</sup>	$\rho$	$6.40 \times 10^3$	$6.09 \times 10^3$
Electric conductivity	$\sigma$	( $\Omega\text{m}$ ) <sup>-1</sup>	$3.26 \times 10^6$	$3.85 \times 10^{6b}$
Prandtl number	Pr		0.027	0.024
Magnetic Prandtl number	P <sub>m</sub>		$1.48 \times 10^{-6}$	$1.36 \times 10^{-6}$

<sup>a</sup>given at 33 °C<sup>b</sup>given at 40 °C

of the magnetic field strength of 5%, whereas the second one achieves a maximum field intensity of 120 mT while the homogeneity of the field intensity is better than 2%.

According to the coordinate system chosen here, the magnetic field is aligned along the  $x$  direction. The physical properties of the test fluids and related nondimensional parameters are summarized in Table I. The calculation of Ra and  $Q$  is performed using these data and the vertical temperature difference between the copper plates  $\Delta T$ , as well as the intensity of the magnetic field  $B$ . Moreover, the constant of the magnetic permeability in vacuum,  $4\pi \times 10^{-7}$  H/m, is used for the calculation of  $Q$ .

The ultrasonic velocity profiling (UVP) and thermocouples were deployed for measuring flow fields and temperature fluctuations, respectively. Three ultrasonic transducers labeled UV1, UV2, and UV3 were mounted on the side wall perpendicular to the magnetic field, whereas one transducer (UV4) was installed at the other side wall and aligned parallel to the magnetic field [Fig. 1(a)]. The ultrasonic Doppler method is based upon the pulse-echo technique and delivers instantaneous profiles of the velocity component projected onto the propagation line of the ultrasonic wave,  $u_y(y, t)$  and  $u_x(x, t)$ , respectively. Further details of the UVP and its application in liquid metal flows can be found in the relevant literature [17, 18]. The vertical temperature difference applied across the fluid layer is determined by thermocouples embedded in the copper plates as  $\Delta T = T_H - T_L$  [Fig. 1(b)]. Additionally, one thermocouple is inserted directly into the fluid layer at a distance of 60 mm from both side walls and 3 mm below the top plate, corresponding to  $x = 60$ ,  $y = 60$ , and  $z = 37$  mm [Fig. 1(b)], to capture the time fluctuations of the temperature arising from the oscillatory motion of the convection rolls.

The following procedure was applied in all experiments: first, the fluid layer was stabilized at a fixed  $Q$  number without applying any vertical temperature difference, namely,  $Ra = 0$ . Then, the Ra number was gradually increased by increasing the heating temperature  $T_H$  at a fixed cooling temperature  $T_L$ . Because of gradually approaching the setting temperature, the most unstable mode of the thermal convection may appear in the fluid layer.

### III. MEASUREMENT RESULTS

#### A. Regime diagram

An essential contribution of the present paper is the extension of the existing regime diagram towards larger

Chandrasekhar numbers up to  $Q = 7.7 \times 10^3$ , where the data series at  $Q = 2.1 \times 10^3$  was obtained at Hokkaido University with liquid gallium as the test fluid. Experiments at higher  $Q$  numbers were conducted at HZDR. Figure 2(a) shows the regime diagram containing data points replotted from Ref. [10] for small Chandrasekhar numbers,  $Q < 2 \times 10^3$ . Assuming that the results of the linear stability analysis by Burr and Müller [11] are applicable for this geometry with aspect ratio of five, the dependence of the critical Rayleigh number for the

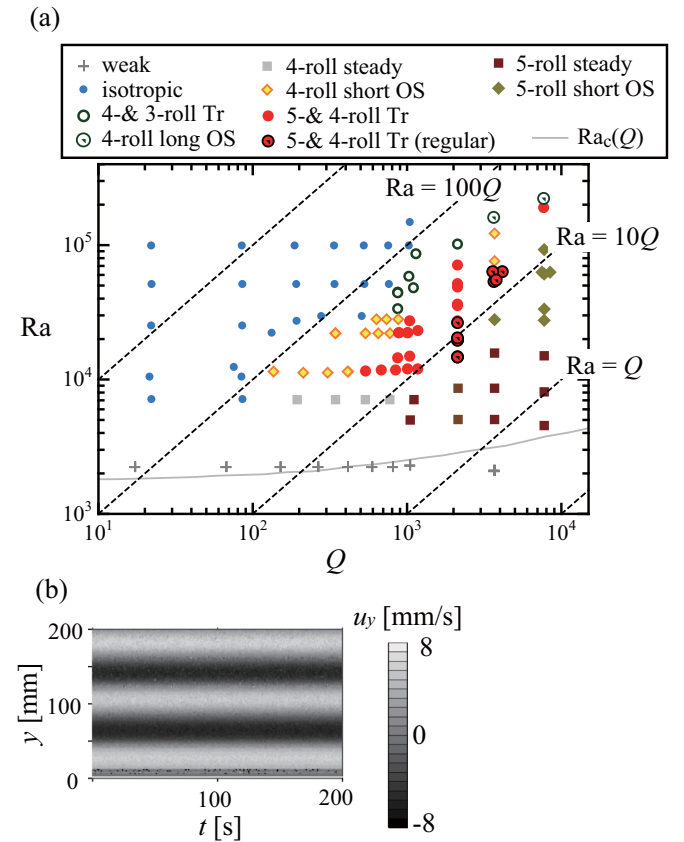


FIG. 2. (a) Regime diagram extended to larger  $Q$  regions, where the gray solid line represents the neutral stability curve given by Burr and Müller [11]; the regimes at smaller  $Q$  than  $2 \times 10^3$  are replotted from Ref. [10]. (b) Spatiotemporal velocity distribution corresponding to a five-roll steady regime obtained at  $Q = 3.7 \times 10^3$  and  $Ra = 1.6 \times 10^4$ .

onset of convection on the Chandrasekhar number is plotted as a gray curve in the figure. Their results also predict that the critical wave number achieves the maximum at  $Q \sim 2 \times 10^4$  for this geometry, which is out of the range of the present study. The diagonal dashed lines represent the contours of  $10^a \times \text{Ra}/Q$  ( $a = 0, 1, 2, \dots$ ). The regimes (distinguished by different symbols) are identified by characteristic features of the dominant convection structures visualized by the UVP: Fig. 2(b) displays an example of the spatiotemporal velocity map obtained by UVP at a Rayleigh number of  $1.6 \times 10^4$  and a  $Q$  number of  $3.7 \times 10^3$ . The number of stripes corresponds to the number of rolls, where the fluid is moving toward the sensor within the black domains and away from the sensor in the white domains, respectively. The map in Fig. 2(b) indicates the existence of five rolls in the fluid layer as the characteristic distinct structure.

In the extended parameter region examined within this study, three new regimes are observed, namely, a five-roll structure showing short-period oscillations [five-roll short oscillation (OS) regime], a transitional regime between a five- and a four-roll structure showing regular flow reversals [five- and four-roll Tr (regular) regime], and a four-roll structure showing long-period oscillations (four-roll long OS regime). In particular, the existence of a five-roll short OS regime was predicted by the numerical simulation [26]. Details of the respective regimes will be explained later. It can be noticed that parameter regions of different flow regimes seem to be separated by lines of  $\text{Ra}/Q$ , as already mentioned in Ref. [10]. Moreover, the fundamental tendency becomes obvious that the wave number of the rolls increases with increasing  $Q$  number (cf. Andreev and Thess [12]). It should be noted here that hysteresis effects can be observed with respect to the transitions between the particular regimes, especially around the transition (Tr) regimes. The regime diagram shown in Fig. 2(a) was obtained by increasing the Ra number, while  $Q$  was kept constant. The scanning of the same parameter region by the procedure of a stepwise reduction of Ra may result in a slightly modified regime diagram.

Figure 3 presents typical temperature fluctuations recorded at the fixed value of  $Q = 3.7 \times 10^3$  for several Ra numbers corresponding to the flow regimes mentioned above. The temperature signal associated with the four-roll short-period oscillation regime is shown for comparison. The respective flow regimes from Figs. 3(a) to 3(d) are (a) five-roll short OS ( $\text{Ra} = 1.6 \times 10^4$ ), (b) five- and four-roll regular Tr ( $\text{Ra} = 6.3 \times 10^4$ ), (c) four-roll short OS ( $\text{Ra} = 1.2 \times 10^5$ ), and (d) four-roll long OS regime ( $\text{Ra} = 1.6 \times 10^5$ ). Figure 3(e) represents a prolonged time series of the temperature fluctuations occurring during the five- and four-roll regular Tr, as shown in Fig. 3(b). Short-period oscillations exist in all cases and become more pronounced and complex at higher Ra numbers because of the loss of two-dimensionality with increasing Ra. Regular low-frequency oscillations with long-period times of about 170 and 1800 s exist in the regimes of four-roll long OS [Fig. 3(d)] and five- and four-roll regular Tr [Fig. 3(e)], respectively. It is obvious to assume various mechanisms to be responsible for generating the distinct flow regimes which exhibit such different time scales.

For further detailed investigation of the short-period oscillations and statistical characteristics of the related short-scale

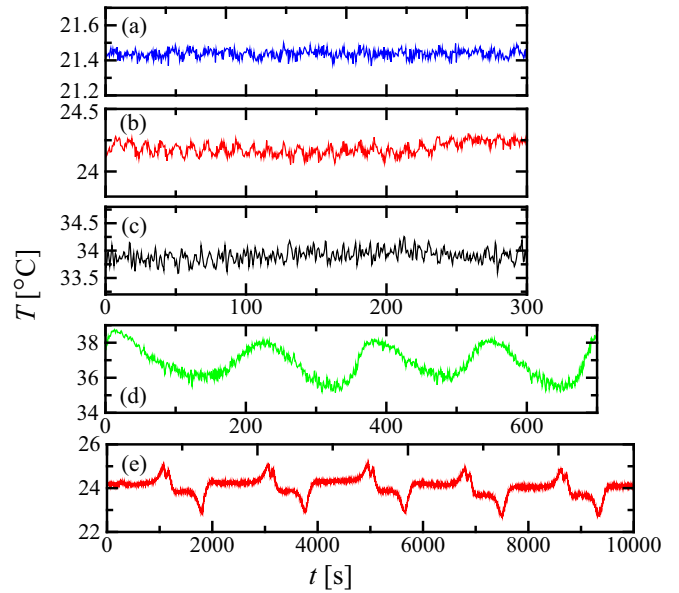


FIG. 3. Typical temperature fluctuations of regimes acquired at  $Q = 3.7 \times 10^3$ : (a) five-roll short period oscillation ( $\text{Ra} = 1.6 \times 10^4$ ), (b) five- and four-roll regular transition ( $\text{Ra} = 6.3 \times 10^4$ ), (c) four-roll short-period oscillation ( $\text{Ra} = 1.2 \times 10^5$ ), and (d) four-roll long-period oscillations ( $\text{Ra} = 1.6 \times 10^5$ ), where (e) represents the prolonged time series of the temperature fluctuation of five- and four-roll regular transition.

temperature fluctuations, the power spectral density (PSD) was calculated from the temperature fluctuations shown in Fig. 3.

From the classical study of Batchelor [27], it is predicted that the developed thermal turbulence in low-Pr number fluids features an inertial subrange and a conductive subrange, which are indicated by slopes of  $-5/3$  and  $-17/3$  in the spectrum, respectively. From a previous study conducted in the same vessel, it is known that developed thermal turbulence is observed at least at  $\text{Ra} \sim 5 \times 10^4$  in the case without magnetic field applied [10]. On the other hand, in the present condition with imposed magnetic field at  $Q = 3.7 \times 10^3$ , the PSDs presented in Fig. 4 do not exhibit any subranges with the corresponding slopes at lower Ra numbers, while the curves seem to approach to the expected slopes with increasing Ra. Small-scale motions are suppressed by the applied magnetic field and the flow does not reach the state of developed thermal turbulence even at  $\text{Ra} = 1.6 \times 10^5$ .

The PSDs show clear peaks for  $\text{Ra} = 1.6 \times 10^4$  (five-roll short OS) and  $\text{Ra} = 6.3 \times 10^4$  (five- and four-roll regular Tr) at frequencies of  $f = 0.073$  and  $0.093$  Hz, respectively. These values correspond to the main frequencies of the short-period oscillations shown in Figs. 3(a) and 3(b). The typical circulation time of a convection roll estimated from the maximum value of the velocity  $u_y(y, t)$  and perimeter of the corresponding circular path line ( $2\pi \times 10$  mm in this case, where 10 mm equals the displacement of the measurement line from the center of the rolls) was found to be about 15.7 s, corresponding to a frequency of 0.06 Hz for  $\text{Ra} = 1.6 \times 10^4$  and 8.2 s (0.12 Hz) for  $\text{Ra} = 6.3 \times 10^4$ . These values are close to the main frequencies appearing in Fig. 4 (0.073 Hz for  $\text{Ra} = 1.6 \times 10^4$  and 0.093 Hz for  $\text{Ra} = 6.3 \times 10^4$ ). The

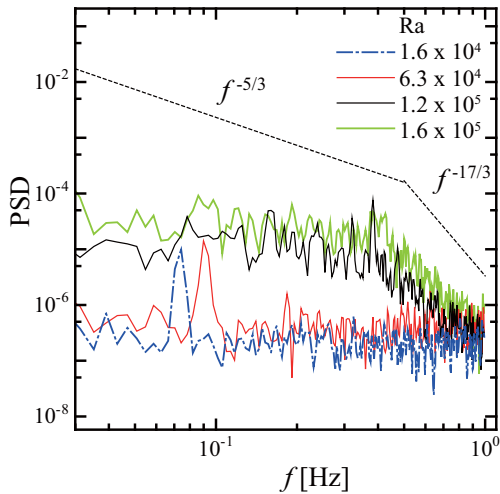


FIG. 4. Power spectral density of the temperature fluctuations shown in Fig. 3 measured at  $Q = 3.7 \times 10^3$ : five-roll short-period oscillation ( $Ra = 1.6 \times 10^4$ ), five- and four-roll regular transition ( $Ra = 6.3 \times 10^4$ ), four-roll short-period oscillation ( $Ra = 1.2 \times 10^5$ ), and four-roll long-period oscillation ( $Ra = 1.6 \times 10^5$ ), where the broken lines show the slopes of  $-5/3$  and  $-17/3$  in the double logarithmic expression.

short-period oscillations in these regimes are assumed to arise from the oscillatory motion of the quasi-two-dimensional convection rolls caused by oscillatory instability, predicted analytically by Clever and Busse [28].

The PSDs for larger  $Ra$  have multiple peak frequencies, while the PSDs for smaller  $Ra$  have single ones. The largest frequency of the multiple peaks at  $Ra = 1.2 \times 10^5$  is  $f_2 = 0.38$  Hz and is about one order of magnitude higher than the main frequencies at smaller  $Ra$  cases. This increase of the peak frequency cannot be explained by a corresponding increase of the circulation time (the estimated frequency is 0.16 Hz). An increase of the  $Ra$  number provokes the development of three-dimensional flow structures. The upcoming three-dimensional character of the flow might start as a partial deformation of the convection cells. For instance, it can be expected that the cell cross sections can become elliptical. The velocity of the convection cells at a radius of 10 mm reaches about 10 mm/s at  $Ra = 1.2 \times 10^5$ . The corresponding circulation time is 6.3 s,

resulting in a frequency of 0.16 Hz. Oscillations arising from a rotating elliptical cell should be detected at  $2 \times 0.16$  Hz, which fits very well with the frequency  $f_1 = 0.32$  Hz in Fig. 4.

**B. “Regular” flow reversals**

In our previous study, irregular, spontaneous flow reversals were observed as temporally irregular transitions between four-roll and five-roll states with reversals of the flow direction inside the rolls. These flow reversals typically occur in a parameter range of  $10 \leq Ra/Q \leq 30$  [9,10]. Within the present study, a different regime is observed in a similar parameter region of  $Ra/Q \sim 10$  [see Fig. 2(a)] at higher  $Q$  numbers: regular transitions between a five- and a four-roll state showing periodic reversals of the roll’s rotational direction. The reversals occur at very regular intervals having a certain time period of  $\sim 1800$  s [see Fig. 3(e)] that is significantly longer than the circulation time of the rolls and the characteristic time of the irregular flow reversals of about 660 s [9]. This regime is represented by red circles with a central dot in the regime diagram in Fig. 2(a).

Figure 5 shows the corresponding spatiotemporal velocity maps of “regular” flow reversals recorded at  $Ra = 5.3 \times 10^4$  and  $Q = 3.7 \times 10^3$ . The measurement lines are perpendicular to the magnetic field lines in Fig. 5(a) [sensor UV2 in Fig. 1(a)] and parallel to the direction of the magnetic field in Fig. 5(b) [sensor UV4 in Fig. 1(a)]. The regime is clearly dominated by the five-roll state, which occupies considerably longer periods of the measurement time than the four-roll state. The four-roll structure can only be detected during a very short time gap, while a reorganization of the five-roll structure proceeds. One can distinguish between two nonequivalent states of the five-roll structure differing in the flow direction within the circulation rolls as well as in their lifespan. Flow measurements at the sensor position UV2 presented in Fig. 5(a) reproduce both states. According to the arrangement of the rolls rotating against each other, white-black-white-black-white and black-white-black-white-black patterns become visible. However, the most striking difference has been revealed by measurements of the velocity component along the convection rolls [see Fig. 5(b) for the sensor position UV4]. Distinct flow structures can be observed here notwithstanding that the flow component parallel to the field lines appears to be

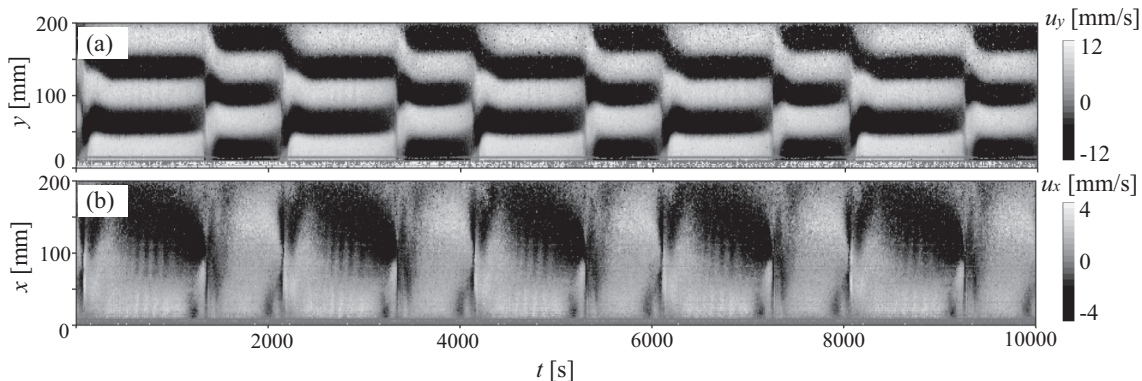


FIG. 5. Spatiotemporal velocity map representing the “regular” flow reversals observed at  $Ra = 5.3 \times 10^4$ ,  $Q = 3.7 \times 10^3$ : (a) direction perpendicular to the magnetic field (sensor UV2 in Fig. 1) and (b) direction parallel to the magnetic field (sensor UV4 in Fig. 1).

significantly smaller around 1/4 or less in comparison to the velocity perpendicular to the magnetic field. It becomes obvious that the flow has a 3D structure all the time. Two characteristic structures of the parallel flow can be detected; their manifestation is clearly related to the associated state of the five-roll structure in the flow perpendicular to the magnetic field. The entire profile of the parallel flow is occupied by a positive velocity without conversion of flow direction during one period of the regular flow reversal, whereas a converging flow towards the center of the fluid cell occurs along the magnetic field lines in the other period. Corresponding to the structures of a single-roll (SR) parallel flow and a double-roll (DR) parallel flow, we label these two stages from now on as the SR state and DR state, respectively. The length of appearance of the DR state and the SR state is expressed by a ratio of approximately 5 : 3. The reason for this asymmetrical flow structure is not clear yet, but the different flow patterns are assumed to be related to the uneven duration of both states of the five-roll structure. A more detailed view of the parallel flow discloses rather complicated flow structures. The position of the collision point of the converging flow during the DR state does not remain stationary. The moment of the flow reversal is signaled by significant changes of the parallel flow before the transition between the five-roll and the four-roll structure becomes apparent in the perpendicular flow. In contrast, the settling time during the SR state seems to be shorter for the perpendicular flow.

Figure 6 compares the spatiotemporal velocity plots obtained perpendicular to the magnetic field at  $Ra = 4.9 \times 10^4$  and  $Q = 3.7 \times 10^3$  by three ultrasonic sensors: UV1 in the left part of the vessel [Fig. 6(a)], UV2 in the center of the vessel [Fig. 6(b)], and UV3 in the right part of the vessel [Fig. 6(c)]. The position of the rolls represented by stripes in the maps remains almost unchanged during longer periods only in the center of the fluid layer [Fig. 6(b)], whereas the convection rolls at the lateral positions UV1 and UV2 move

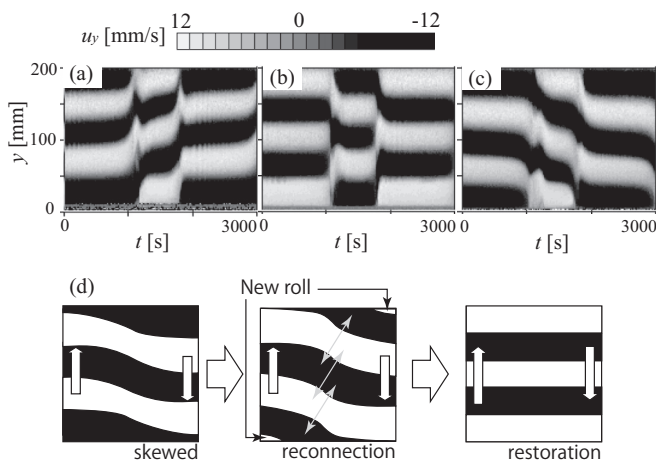


FIG. 6. Spatiotemporal velocity distributions recorded in the five- and four-roll regular Tr regime ( $Ra = 4.9 \times 10^4$ ,  $Q = 3.7 \times 10^3$ ) obtained at different measurement lines in the vessel: (a) UV1 located at top left as shown in the schema, (b) UV2 located at bottom middle, (c) UV3 located at top right, and (d) expected process of roll motions toward the flow reversal in the horizontal plane.

in the opposite direction, as shown in Figs. 6(a) and 6(c). This result indicates a global horizontal circular advection of the rolls during the regime of regular flow reversals, as schematically shown in Fig. 6(d). The horizontal movement of rolls leads to a recurring disappearance of a roll near the lateral wall accompanied by a reconnection of remaining rolls at the central region of the vessel. Then, a rapid growth of additional rolls from the opposite side wall restores the five-roll state with opposite circulation direction. This manifestation of the regime of regular flow reversals shows some striking similarities with recent numerical simulations by Yanagisawa *et al.* [26]. The numerical results revealed the process of flow reversals by the shrinking, bending, and reconnection of the circulation rolls. However, the numerical calculations do not predict such a strict regularity of the reversals as observed in the experiment. Moreover, such an asymmetric behavior of the two states of the five-roll structure as described above (see Fig. 5) is not reported by the numerical study. The direction of the horizontal circulation in regular flow reversals is unchanged (clockwise in this case), while that of the numerical simulation changes. A possible reason could be the fact that the previous numerical simulations published so far [26] were limited to lower Chandrasekhar numbers up to  $Q = 1 \times 10^3$ . As shown in Fig. 6, five rolls in the DR state seem to stably exist with long duration time just after the reconnection. This state shows only a gradual displacement, while the convection rolls in the SR state move continuously with a faster speed. The different behavior of the rolls in both arrangements also becomes visible in Fig. 5(b). Moreover, it should be noticed that the process of relocation of the rolls is obviously more pronounced for measuring positions outside the center of the fluid vessel. Figure 7(a) shows time variations of roll boundaries extracted from the spatiotemporal velocity distribution shown in Fig. 6(a) as a zero-crossing point of the instantaneous velocity profiles. Figure 7(b) is the corresponding double logarithmic graph. As demonstrated by the slopes in the figure, the variations of the roll boundaries in each state are characterized by two different time scales. The roll displacement is accelerated while approaching the moment of reconnection.

Yanagisawa *et al.* [9,26] explained the process of irregular flow reversals as the creation of new rolls (increasing the number of rolls,  $n$ ) and the following skewed-varicose instability with global horizontal circulation (decreasing  $n$ ).

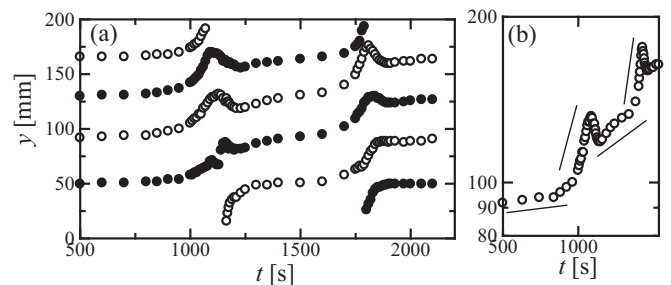


FIG. 7. (a) Time variations of roll boundaries extracted from the spatiotemporal velocity distribution shown in Fig. 6, (a) as the zero-crossing point on the instantaneous velocity profiles and (b) as a double logarithmic expression of the variation.

With the roll number transition, the convection satisfies the condition of a noninteger number as the time average [10]. In this sense, the time-averaged number of rolls corresponding to parameter space in the regime diagram, where this regular flow reversal occurs, is very close to  $n = 5$ . Therefore, the stability of the five-roll arrangement is relatively high, implying a small growth rate of the skewed-varicose instability. This assumption is consistent with the relatively longer period found for the regular reversals in comparison with irregular ones, but it still cannot explain the different behavior of the two arrangements of rolls (DR and SR state).

The flow reversals are not isolated cases restricted to the present configuration of aspect ratio of five because such events are observed in numerical simulations at  $Q = 1 \times 10^3$  [26] for other aspect ratios larger than four. Furthermore, the horizontal circulation for aspect ratios larger than eight is not always a single circulation on the vessel scale; instead, several local circulations can occur. Namely, the flow reversals by a large single circulation are expected to occur in a limited range of the aspect ratio.

#### IV. MODE ANALYSIS BY PROPER ORTHOGONAL DECOMPOSITION

To extract the spatiotemporal characteristics of the regimes observed within this study and inserted in the regime diagram shown in Fig. 2(a), we performed a snapshot proper orthogonal decomposition (snapshot POD) [29] on the spatiotemporal velocity maps obtained by UVP. Because the UVP technique delivers linear profiles of the velocity field, the POD can be considered as a suitable tool to extract coherent flow structures from the measured data [30,31]. Another aspect is the large deformation of the confined roll structure in this vessel with a moderate aspect ratio of 5, in comparison to ideal unbounded conditions. Therefore, common Fourier transform based analysis cannot extract meaningful structures. Furthermore, performing POD on the velocity map will remove unorganized measurement noise caused by, for example, a potential lack of tracer particles in the measuring volume. In POD, orthogonal functions  $\phi(y)$  are determined by maximizing correlation with  $u_y(y, t)$  as

$$\lambda = \frac{\langle \overline{u_y}, \phi \rangle}{\langle \phi, \phi \rangle}, \quad (1)$$

where the angle bracket  $\langle \rangle$  and the overline mean the inner product and the time average, respectively. This problem is converted into an eigenvalue problem of covariance matrix,  $\mathbf{R}(y, y') = u_y(y, t)u_y(y', t)$ , as

$$\mathbf{R}\Phi = \Lambda\Phi, \quad (2)$$

where  $\Phi$  and  $\Lambda$  are the eigenvector matrix consisting of orthogonal functions (or eigenfunctions)  $\phi_i(y)$  and the eigenvalue matrix representing the correlation  $\lambda_i$  for each mode  $i$ . Using  $\phi_i(y)$ ,  $u_y(y, t)$  is decomposed into

$$u_y(y, t) = \sum_{i=1}^m A_i(t)\phi_i(y), \quad (3)$$

where  $A_i(t)$  is the amplification coefficient which reconstructs the original velocity maps from the normalized eigenvector

and represents the instantaneous correlation between  $u_y(y, t)$  and  $\phi_i(y)$ . To evaluate the contribution rate of the mode  $i$  to the whole system, the normalized energy fraction

$$E_i = \frac{\lambda_i}{\sum_{i=1}^m \lambda_i} \quad (4)$$

has been commonly used. The number of modes is determined by the number of spatial data points, which was around 200 in the present measurements. In [32], POD was applied for three-dimensional simulations of nonmagnetic, turbulent RBC in a finite layer. The dominant modes in that case are more complex, while in the present cases dominant modes are rather generic, reflecting the quasi-two-dimensionality of the structure.

#### A. Regular flow reversals

Figure 8 shows the results of the POD analysis of the spatiotemporal velocity map for the regime of regular flow reversals (five- and four-roll regular Tr) measured at  $Ra = 4.9 \times 10^4$  and  $Q = 3.6 \times 10^3$  by UV1. The measurement line is directed perpendicular to the magnetic field and placed

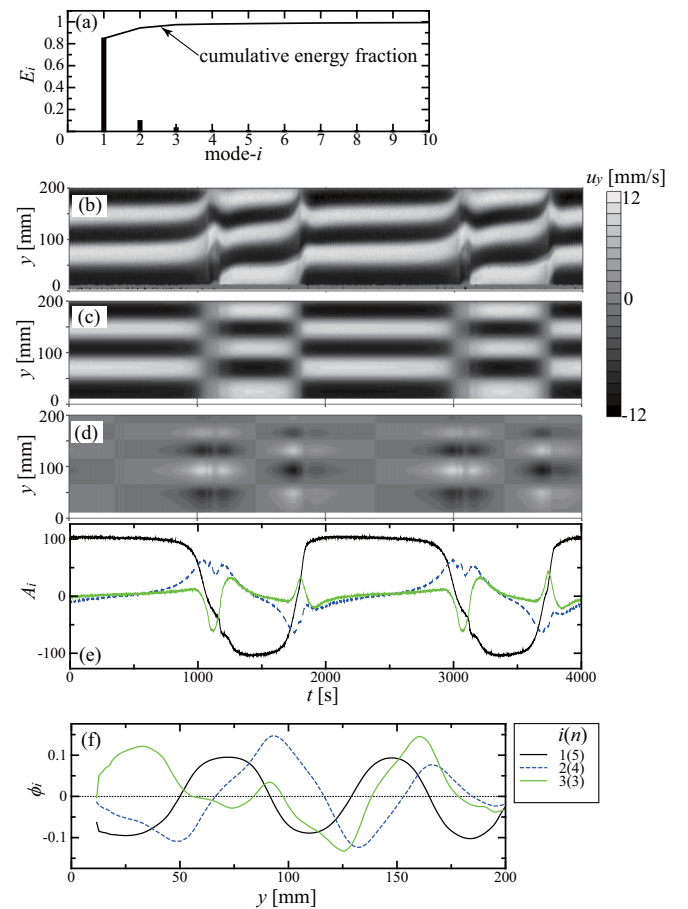


FIG. 8. Snapshot POD analysis of the spatiotemporal velocity distribution corresponding to the “regular flow reversals” measured at  $Ra = 4.9 \times 10^4$ ,  $Q = 3.6 \times 10^3$  by UV1: (a) energy fraction at each mode, (b) original spatiotemporal velocity distribution, (c) spatiotemporal distributions of first and (d) second POD mode, (e) temporal energy fluctuations, and (f) eigenfunctions of first three modes, where  $n$  is the corresponding number of rolls.

at a distance of 40 mm from the left side wall [see Fig. 1(a)]. Here, Figs. 8(a) to 8(f) correspond to (a) energy fraction  $E_i$  and cumulative fraction, (b) original spatiotemporal velocity map, (c) POD first mode and (d) second mode, (e) energy fluctuation  $A_i(t)$ , and (f) profiles of eigenfunctions,  $\phi_i(y)$ , for the first three modes,  $i = 1$  to 3, respectively. As shown in Fig. 8(a), the first and second modes occupy around 96% of the total energy ( $E_1 = 78.8\%$ ,  $E_2 = 17.1\%$ ). These modes correspond to the five-roll ( $n = 5$ ) and the four-roll ( $n = 4$ ), respectively. The results suggest that the regular flow reversals can be considered as a periodic competition between the five- and four-roll states [Figs. 8(c) and 8(d)]. Namely, the four-roll state gradually grows with a gradual decay of the five-roll state. This correlation is represented by  $A_i(t)$  as defined in Eq. (3) and is shown in Fig. 8(e). Likely the third mode represents the three-roll state, as displayed in Fig. 8(f), but the corresponding eigenfunction shows a fluctuating behavior and the mode contains a fraction of only 3% with respect to the total energy.

Figure 9 shows the POD results of the spatiotemporal velocity distribution measured by the transducer UV3 [see Fig. 1(a) for sensor position] simultaneously with the data presented in Fig. 8(b) (sensor UV1). The graphs display the spatiotemporal velocity distributions of the original data [Fig. 9(a)], as well as the first [Fig. 9(b)] and the second [Fig. 9(c)] POD mode. The manifestation of the first mode appears to be very similar to the pattern obtained for the measurement line UV1 shown in Fig. 8(c). The second mode behaves similar too [Figs. 8(d) and 9(c)], but the comparison of both patterns for UV1 and UV3 reveals an opposite sign of the velocity direction at any time, while the first mode shows a unidirectional flow at both measuring positions [Figs. 8(c) and 9(b)]. It reflects a skewed state of the four-roll structure, as schematically shown in Fig. 6(d).

### B. Irregular flow reversals

Irregular flow reversals as reported in Yanagisawa *et al.* [9,10] are also observed in the parameter region examined in this study. The respective measurements are represented

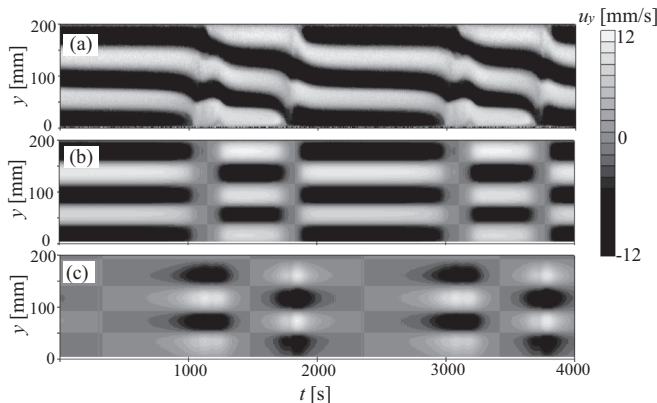


FIG. 9. Snapshot POD analysis of the spatiotemporal velocity distribution measured by transducer UV3 simultaneously with the data shown in Fig. 8(b): spatiotemporal velocity distributions of (a) original data, (b) first and (c) second POD mode.

by small circular symbols in the regime diagram shown in Fig. 2(a). We also performed the POD analysis of the spatiotemporal velocity map for irregular flow reversals recorded at  $Ra = 4.8 \times 10^4$  and  $Q = 2.1 \times 10^3$ . Figure 10(b) contains the results for the measurement line of transducer UV1. This velocity map was measured at Hokkaido University in liquid gallium. The horizontal white lines in the spatiotemporal plot represent measurement errors arising from multiple reflections of the ultrasonic wave. These artifacts were also observed in previous studies [9,10], but their consequences on further data processing are not critical and do not pose a serious problem for analyzing the flow structure. The energy shown in Fig. 10(a) divides up into a much broader distribution on the particular modes, as shown in Fig. 8(a) for the case of the regular flow reversals. This result indicates that multiple modes play an influential role in the context of irregular flow reversals. The first mode corresponding to the four-roll state ( $n = 4$ ) [Fig. 10(c)] contains only 52.2% of the total energy, whereas the cumulative energy exceeds 95% at the twenty-second

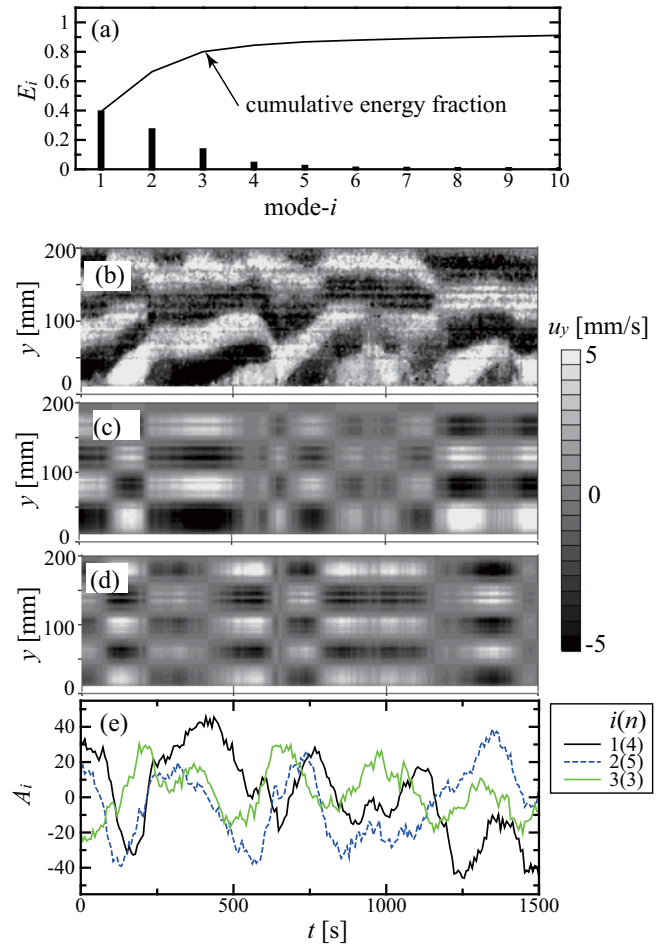


FIG. 10. Snapshot POD analysis of spatiotemporal velocity distribution corresponding to the “irregular flow reversals” measured at  $Ra = 4.8 \times 10^4$  and  $Q = 2.1 \times 10^3$  by UV1 as the measurement line: (a) eigenvalue spectra, (b) original spatiotemporal velocity distribution, (c) spatiotemporal distribution of first and (d) second POD mode, and (e) temporal energy fluctuations of the first three modes.

mode. The second mode corresponds to the five-roll state ( $n = 5$ ) [Fig. 10(d)] and displays a complementary behavior with respect to the first mode. This is also represented as  $|A_1(t)|$  and  $|A_2(t)|$ , which are temporal energy fluctuations of the first and second modes shown in Fig. 10(e). This observation is similar to the competition between the five-roll and the four-roll states occurring during the regular flow reversals (Fig. 8). According to the profiles of the eigenfunctions  $\phi_i(y)$ , the following third, fourth, and fifth modes correspond to the third-, sixth-, and seventh-roll states, respectively. From comparison between the irregular and regular flow reversals, it becomes obvious that the four-roll state as the dominating mode observed in irregular flow reversals shows an unstable and fluctuating roll structure. The POD analysis indicates that fluctuations and irregularities arise from the broad appearance of the multiple-roll states. This is a crucial difference from the random flow reversals of large scale circulations (LSC) in vessels with relatively small aspect ratios (around unity), where the randomness is driven by thermal turbulence.

### C. Long- and short-period oscillations

Besides the phenomena of flow reversals, long- and short-period oscillations of quasi-two-dimensional rolls were observed in the present experiments [see also Fig. 2(a)]. Here, we aim to extract the characteristics of the oscillations from the spatiotemporal velocity map by means of the POD analysis. Figure 11 shows the results of the POD analysis of the velocity map related to the four-roll long-period oscillations measured at  $Ra = 1.6 \times 10^5$ ,  $Q = 3.7 \times 10^3$  (measurement line UV1). The energy fraction spectrum in Fig. 11(a) and the spatiotemporal map of the first and second modes shown in Figs. 11(c) and 11(d) demonstrate that the oscillation [original velocity map is shown in Fig. 11(b)] consists of a dominant four-roll state and a minor three-roll state, where the first mode represents 89.5% of the total energy and the second mode contributes with a fraction of 6.2% to the total energy. An assessment of the instantaneous intensity of modes can be done by an instantaneous correlation between each POD mode and the original velocity profile. This is represented by periodic variations of  $|A_i(t)|$  in Fig. 11(e) being similar to the temporal competition between five- and four-roll states in the regular flow reversals shown in Fig. 8(e). In this sense, the four-roll long-period oscillation seems to fall in essentially the same category of a four- and three-roll transition reported by Yanagisawa *et al.* [10]. Both regimes can be observed at almost the same ratio of  $Ra/Q$ , as shown in Fig. 2(a). The main difference is a minor decrease of energy of the four-roll state transferring to the three-roll state, which is not enough to achieve an alternating arrangement of counter-rotating rolls as observed for the situation of the flow reversals. The rolls in this regime also exhibit short-period oscillations, as discussed in Sec III A and in Fig. 3. But unlike the long-period oscillation, the fluctuating components of the short-period oscillations are fed by multiple modes, as shown in Fig. 11(e), and cannot be decomposed into a single mode. It means that the short-period oscillation has no clear spatial mode, unlike the long-period one.

We also examined the five-roll short-period oscillation which has been observed in the present experiments. The

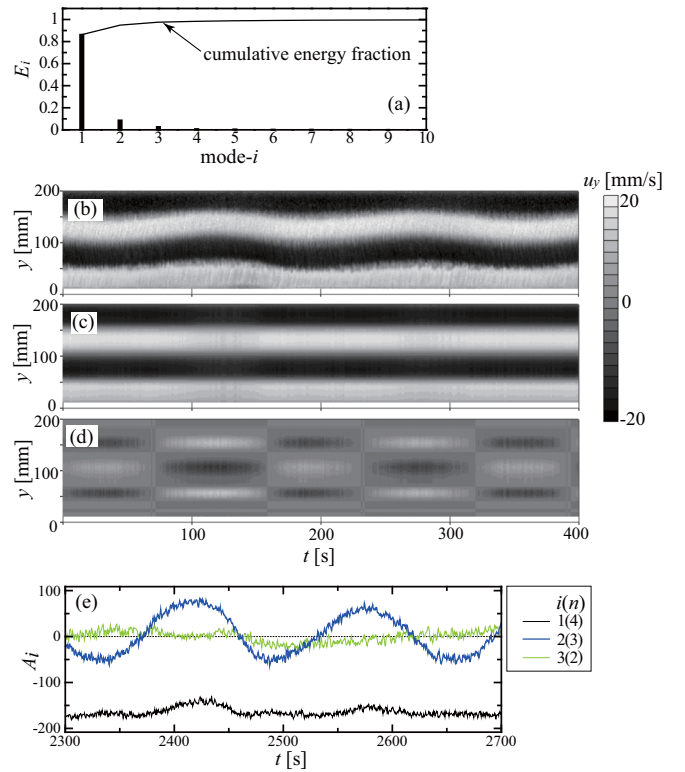


FIG. 11. Snapshot POD analysis of spatiotemporal velocity distribution corresponding to the “long-period oscillation” measured at  $Ra = 1.6 \times 10^5$ ,  $Q = 3.7 \times 10^3$  by UV1: (a) eigenvalue spectra, (b) original spatiotemporal velocity distribution, (c) spatiotemporal distribution of first and (d) second POD mode, and (e) temporal energy fluctuations of first three eigenmodes, where  $n$  is the corresponding number of rolls for each mode.

original spatiotemporal velocity map shown in Fig. 12(b) was measured at  $Ra = 2.8 \times 10^4$  and  $Q = 3.7 \times 10^3$  by the transducer UV1. The dominant mode in the POD analysis corresponds to the five-roll state and occupies 98.3% of the total energy [Figs. 12(a) and 12(c)]. The following second mode contains only 0.1% of the total energy, but it represents the short-period oscillations of the rolls as a single-roll state,  $n = 1$  [Figs. 12(a), 12(d), 12(e)]. In particular, the short-period oscillation in this regime can be considered as a shaking of the quasisteady rolls over the vessel. There is no correlation between  $|A_1(t)|$  and  $|A_2(t)|$ , unlike the long-period oscillations.

### D. Effective roll numbers

As explained in the section above, the spatiotemporal velocity map of each regime can be decomposed by POD analysis into various modes representing different numbers of rolls. In this section, we propose an evaluation procedure to determine the effective roll number based on the POD analysis. A manual detection of the instantaneous number of rolls in our previous study [10] revealed that the time-averaged number of rolls continuously varies with increasing  $Ra$  for a fixed value of  $Q$ . The present procedure will provide more objective information about the effective number of rolls. The effective roll number  $N_e$  is calculated based on energy fraction  $E_i$  and

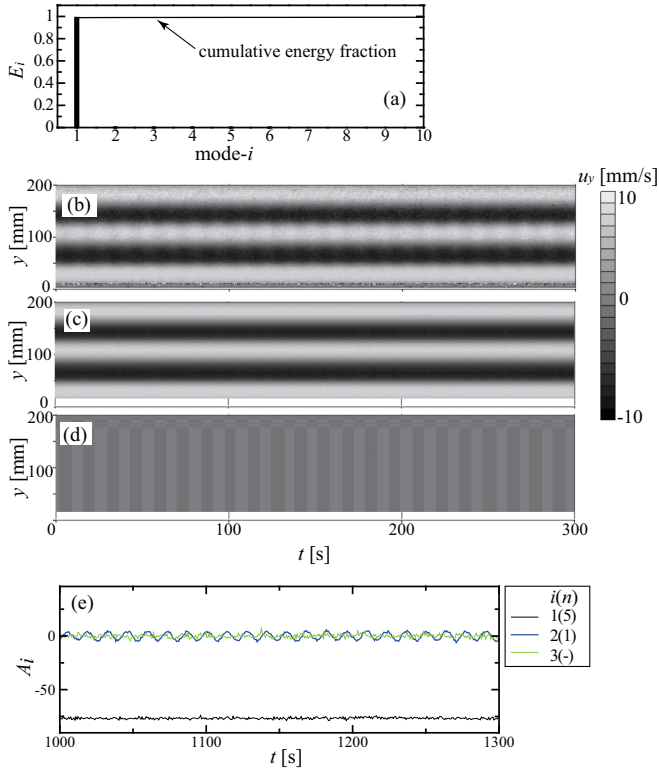


FIG. 12. Snapshot POD analysis of the spatiotemporal velocity distribution corresponding to the “five-roll oscillation” measured at  $Ra = 2.8 \times 10^4$ ,  $Q = 3.7 \times 10^3$  by UV1: (a) eigenvalue spectra, (b) original spatiotemporal velocity distribution, (c) spatiotemporal distribution of first and (d) second POD mode, and (e) temporal energy fluctuations of first three eigenmodes, where  $n$  is the corresponding number of rolls for each mode.

the numbers of rolls of each mode  $n_i$  as

$$N_e = \frac{\sum_{i=1}^m E_i n_i}{\sum_{i=1}^m E_i}, \quad (5)$$

where  $m$  is the number of modes that satisfies the following criteria: (i) the profile of its eigenfunction clearly represents the number of rolls  $n_i$ , and (ii)  $E_i$  is larger than 0.1%. Figure 13 displays the results from an evaluation of all experimental data obtained in the present study at three different numbers of  $Q$ :  $Q = 2.1 \times 10^3$ ,  $3.7 \times 10^3$ , and  $7.7 \times 10^3$ , with increasing  $Ra$ , where the symbols indicate the corresponding flow regime according to Fig. 2(a).  $N_e$  is drawn against  $Ra/Q$ , and  $k$  is the corresponding dimensionless wave number of the respective roll pattern. Figure 13 illustrates a monotonic decrease of  $N_e$  with increasing  $Ra/Q$  from  $N_e = 5$  to 4 and values below. Although different flow regimes appear with increasing ratio  $Ra/Q$ , the variations of  $N_e$  obey a uniform tendency. Regular flow reversals are observed around  $N_e = 5$ , while irregular reversals are found at intermediate values of  $N_e$  between 5 and 4. The regime of four rolls with long-period oscillations occurs around  $N_e = 4$ . Irregular reversals between four- and three-roll states exist at effective roll numbers slightly below 4. It is worthwhile to note that the roll motion is quasiregular near the integer numbers of  $N_e$ , whereas irregularities become manifest if the effective roll number  $N_e$  deviates significantly

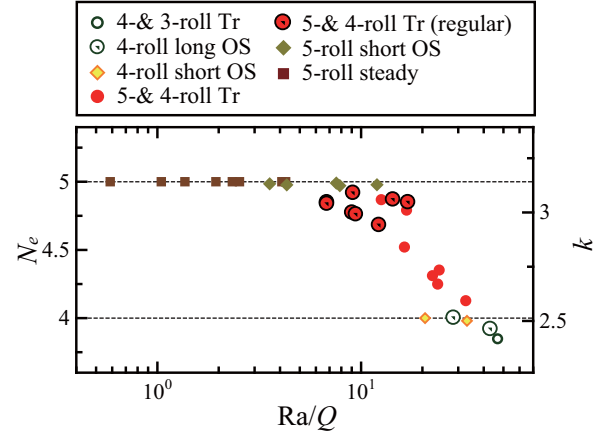


FIG. 13. Effective roll number evaluated by POD analysis,  $N_e$  (and corresponding nondimensional wave number  $k$ ), vs  $Ra/Q$ , with increasing  $Ra$  at fixed values of  $Q = 2.1 \times 10^3$ ,  $3.7 \times 10^3$ , and  $7.7 \times 10^3$ , where the symbols represent the corresponding regimes summarized in Fig. 2(a).

from an integer value. Namely, in the case of five- and four-roll transitions, the flow reversals show distinct irregular features if the parameters exceed the value of  $Ra/Q = 10$  that corresponds to the condition  $N_e = 5$ .

## V. CONCLUSIONS

In the present study, we extended the regime diagram of Rayleigh-Bénard convection affected by a horizontal magnetic field to larger  $Q$  and  $Ra$  regions in comparison with Yanagisawa *et al.* [10]. The experimental results confirmed the suggestion of our previous study that a qualitative classification of flow regimes can be carried out by dividing the regime diagram into different  $Ra/Q$  zones. Three regimes were identified. In particular, a regime of regular flow reversals was found as a form of periodic transitions between a five- and a four-roll state. The regular reversals are observed in a similar  $Ra/Q$  range as reported for irregular flow reversals [9,10], where four- and five-roll states switch irregularly accompanied by an inversion of flow direction in the rolls. Multiple line measurements of the spatiotemporal velocity field in the vessel suggest the assumption that the regular flow reversals are caused by a horizontal circular advection of the rolls. Two separate states were identified within the regime of regular reversals. Besides the opposite rotational sense of the rolls, these states differ in the flow structure appearing in the direction parallel to the magnetic field and the lifespan. It becomes obvious that the global flow structure in the regime of the regular reversals is always three dimensional.

POD analysis provides important insights as a basis for a more detailed description of the flow regimes. Regular flow reversals are represented by a periodic competition between the major five-roll state and the minor four-roll state. In contrast, in the irregular flow reversals, multiple modes having a different number of rolls contain considerable fractions of energy besides the dominating four-roll and minor five-roll states. Short-period oscillations of the five-roll state are identified as an oscillating single roll, whereas the long-period oscillations

of the four-roll state are caused by a periodic growth and decay of the three-roll state. The effective roll number  $N_e$  was determined by a POD analysis based on the energy fraction of the substantial modes. This approach provides a more objective representation of the average roll number in comparison to a time average of the instantaneous roll number. Variations of  $N_e$  obtained at different values of  $Q$  against  $Ra/Q$  show the same behavior. Regular flow reversals occur at  $N_e \sim 5$  and irregular ones at intermediate values of  $4 < N_e < 5$ . We conclude that disorders of the irregular flow reversals do not arise from the randomness of turbulence like the reversals of LSC, but from the instability of the quasi-two-dimensional rolls, which becomes apparent by a more stochastic appearance of multiple modes.

The key mechanism for time variations observed here is the interaction between the convection rolls and vessel-scale

horizontal circulations in a confined geometry. The present case is determined by a quasi-two-dimensional restriction on the convection rolls imposed by a sufficiently strong horizontal magnetic field. An important further extension towards a deeper understanding of the spontaneous, repetitive transition of large scale convection structures might be the consideration of other geometries and aspect ratios, which might be addressed in subsequent experiments or numerical simulations.

#### ACKNOWLEDGMENTS

This work was supported by JSPS KAKENHI Grant No. 24244073. The authors express thanks for this support. The authors from HZDR acknowledge the financial support in the framework of the Helmholtz alliance “LIMTECH.”

- 
- [1] E. Bodenschatz, W. Pesch, and G. Ahlers, *Ann. Rev. Fluid Mech.* **32**, 709 (2000).
  - [2] G. Ahlers, S. Grossmann, and D. Lohse, *Rev. Mod. Phys.* **81**, 503 (2009).
  - [3] D. Lohse and K.-Q. Xia, *Ann. Rev. Fluid Mech.* **42**, 335 (2010).
  - [4] E. L. Koschmieder, *Bénard Cells and Taylor Vortices* (Cambridge University Press, Cambridge 1993).
  - [5] M. Lappa, *Thermal Convection: Patterns, Evolution and Stability* (Wiley, New York, 2010).
  - [6] K. R. Sreenivasan, A. Bershadskii, and J. J. Niemela, *Phys. Rev. E* **65**, 056306 (2002).
  - [7] K. Sugiyama, R. Ni, R. J. A. M. Stevens, T. S. Chan, S.-Q. Zhou, H.-D. Xi, C. Sun, S. Grossmann, K.-Q. Xia, and D. Lohse, *Phys. Rev. Lett.* **105**, 034503 (2010).
  - [8] R. Ni, S.-D. Hung, and K.-Q. Xia, *J. Fluid Mech.* **778**, R5 (2015).
  - [9] T. Yanagisawa, Y. Yamagishi, Y. Hamano, Y. Tasaka, and Y. Takeda, *Phys. Rev. E* **83**, 036307 (2011).
  - [10] T. Yanagisawa, Y. Hamano, T. Miyagoshi, Y. Yamagishi, Y. Tasaka, and Y. Takeda, *Phys. Rev. E* **88**, 063020 (2013).
  - [11] U. Burr and U. Müller, *J. Fluid Mech.* **453**, 345 (2002).
  - [12] O. Andreev and A. Thess, *Phys. Fluids* **15**, 3886 (2003).
  - [13] S. Chandrasekhar, *Hydrodynamic and Hydromagnetic Stability* (Oxford University Press, Oxford, 1961).
  - [14] P. A. Davidson, *J. Fluid Mech.* **299**, 153 (2006).
  - [15] F. H. Busse and R. M. Clever, *J. Theor. Appl. Mech.* **2**, 495 (1983).
  - [16] S. Fauve, C. Laroche, and A. Libchaber, *J. Phys. Lett.* **42**, 455 (1981).
  - [17] B. Birkhofer, N. Furuichi, T. Kawaguchi, H. Kikura, H. Minagawa, M. Mori, Y. Murai, H. Murakawa, M. Motozawa, S. Nahar *et al.*, in *Ultrasonic Doppler Velocity Profiler for Fluid Flow*, Vol. 101, edited by Y. Takeda (Springer, New York, 2012).
  - [18] S. Eckert, A. Cramer, and G. Gerbeth, in *Magnetohydrodynamics - Historical Evolution and Trends*, edited by S. Molokov, R. Moreau, and H. K. Moffatt (Springer, Berlin, 2007), p. 275.
  - [19] T. Mashiko, Y. Tsuji, T. Mizuno, and M. Sano, *Phys. Rev. E* **69**, 036306 (2004).
  - [20] Y. Tsuji, T. Mizuno, T. Mashiko, and M. Sano, *Phys. Rev. Lett.* **94**, 034501 (2005).
  - [21] N. B. Morley, J. Burris, L. C. Cadwallader, and M. D. Nornberg, *Rev. Sci. Instrum.* **79**, 056107 (2008).
  - [22] Y. Plevachuk, V. Sklyarchuk, S. Eckert, G. Gerbeth, and R. Novakovic, *J. Chem. Eng. Data* **59**, 757 (2014).
  - [23] K. Okada and H. Ozoe, *J. Heat Trans.* **114**, 107 (1992).
  - [24] K. E. Spells, *Proc. Phys. Soc.* **48**, 299 (1936).
  - [25] W. H. Cubbery, in *Metals Handbook*, Vol. 2, edited by H. Baker (ASM International, Metals Park, Ohio, 1979), p. 735.
  - [26] T. Yanagisawa, Y. Hamano, and A. Sakuraba, *Phys. Rev. E* **92**, 023018 (2015).
  - [27] G. K. Batchelor, *J. Fluid Mech.* **5**, 134 (1959).
  - [28] R. M. Clever and F. H. Busse, *J. Fluid Mech.* **176**, 403 (1987).
  - [29] L. Sirovich, *Quart. Appl. Math.* **45**, 561 (1987).
  - [30] Y. Takeda, *J. Fluid Mech.* **389**, 81 (1999).
  - [31] N. Furuichi, Y. Takeda, and M. Kumada, *Exp. Fluids* **34**, 643 (2003).
  - [32] J. Bailon-Cuba and J. Schumacher, *Phys. Fluids* **23**, 077101 (2011).